RADIATION AND FAST NEUTRON SHIELDING PROPERTIES OF NILO ALLOY

Sunantasak Ravangvong[1,*], Punsak Glumglomchit[2], Chaiyasit Kasorn[2], Natcharee Huekharnjiraroj[2], Panthita Sakha[2], Ravitnipha Kanuenghet[2] and Kittisak Sriwongsa[3,4]

Received: August 05, 2024; Revised: December 03, 2024; Accepted: January 13, 2025

Abstract

Nowadays, alloy materials have become increasingly important in radiation shielding due to their high density, which is crucial for effective radiation attenuation. The goal of this study was to evaluate several radiation shielding parameters, including the mass attenuation coefficient (MAC), half value layer (HVL), tenth value layer (TVL), and mean free path (MFP) for Nilo alloys 36, 42, and 48. These evaluations were conducted across a photon energy range of 1 keV to 100 GeV using the WinXCom software. Additionally, buildup factors (EABF and EBF) were simulated using the geometric progression (G-P) fitting method for energies ranging from 0.015 to 15 MeV, at depths corresponding to 1-40 mean free paths (mfp). Furthermore, fast neutron removal cross sections (ΣR) were determined using the partial density method for energies between 2 and 12 MeV. The results showed that Nilo alloy 48 exhibited the highest MAC and ΣR values, while its HVL, TVL, and MFP were the lowest among the samples. When comparing HVL, TVL, and MFP values of the Nilo alloys to hematite serpentine, it was found that all the Nilo alloy samples had lower values than hematite serpentine. These findings suggest that Nilo alloy 48 offers excellent radiation and fast neutron shielding, making it a promising candidate for the development of lead-free shielding materials.

Keywords: **Alloy; Fast neutron shielding; Mass attenuation coefficient; Radiation shielding**

[1] *Division of Science and Technology, Faculty of Science and Technology, Phetchaburi Rajabhat University, Phetchaburi, Thailand. E-mail: sunantasak.rav@mail.pbru.ac.th**

[2] *Huahinvitthayalai School, Hua-Hin, Prachuap Khiri Khan, Thailand. E-mail: punsakk@gmail.com; chantimakasorn@gmail.com; ideaiooniam@gmail.com; fofee2808@gmail.com; rawitnipha@gmail.com*

[3] *The demonstration school of Silpakorn University, Nakhon Pathom, Thailand. E-mail: sriwongsa_k@silpakorn.edu*

[4] *Education Program in Physics, Faculty of Education, Silpakorn University, Nakhon Pathom, Thailand.*

[*] *Corresponding author*

DOI: https://doi.org/10.55766/sujst-2024-06-e06050

Introduction

The development of new materials plays a crucial role in advancing technology. Multi-component materials such as superconductors, composites, biomaterials, semiconductors, polymers, and alloys are gaining significant attention across various fields, including bioengineering, microelectronics, space technology, energy, construction, and transportation (Fernandes *et al*., 2021; Padhy *et al*., 2024; Saleh *et al*., 2024). Alloys, in particular, are widely used in industries such as biomedical, pharmaceuticals, aerospace, transportation, and radiation shielding due to their high tensile strength, hardness, corrosion resistance, and environmental friendliness, making them less toxic compared to lead (Saleh *et al*., 2022; Wu *et al*., 2023). Nilo alloys, a family of multi-compound alloys primarily composed of nickel and iron (Ni-Fe), are known for their low thermal expansion, good ductility, and excellent strength and toughness (Padhy *et al*., 2024).

In dosimetry and radiation shielding, materials with high corrosion resistance, mechanical strength, atomic numbers, and density are essential (Kursun *et al*., 2023; Aldawood *et al*., 2024; Yaykaşlı *et al*., 2023; Wu *et al*., 2023). Nickel-based alloys are commonly used in devices such as turbines, heat exchangers, and rocket motors due to their resistance to oxidation, high-temperature performance, and magnetic properties (Ekinci *et al*., 2021; Liu *et al*., 2024a; Cheng *et al*., 2024), as well as in the development of radiation shielding materials (Aygün, 2021). Iron-based alloys, on the other hand, are known for their cost-effectiveness, excellent soft magnetic properties, better wettability, and environmental friendliness. These features make them widely used in devices like transformers, motors, generators, and relays (Huang *et al*., 2024; Khakwani, 2024; Liu *et al*., 2024b). The exceptional microstructural stability at intermediate temperatures, high creep strength, good corrosion resistance, and relatively low cost of Ni-Fe alloys make them highly promising for a variety of applications (Xu *et al*., 2023; Pan *et al*., 2024). Nilo alloys, which are composed of varying amounts of nickel and iron (e.g., Nilo 36, 42, and 48), are known for their high density compared to hematite serpentine concrete. This property is particularly important in radiation shielding applications.

In this study, the radiation and fast neutron shielding properties of Nilo alloys 36, 42, and 48 were analyzed. Radiation shielding parameters such as the mass attenuation coefficient (MAC), half value layer (HVL), tenth value layer (TVL), and mean free path (MFP) were evaluated using the WinXCom software over a photon energy range of 1 keV to 100 GeV. Additionally, buildup factors were estimated using the geometric progression (G-P) fitting method for energies ranging from 0.015 to 15 MeV, at depths corresponding to 1-40 mean free paths (mfp). Fast neutron removal cross sections (ΣR) were also determined using the partial density method, with an energy range of 2 to 12 MeV. The resulting data were analyzed in relation to the chemical compositions of the alloys to assess their shielding effectiveness.

Materials and Methods

Table 1 displays the results of this work, the various chemical compositions, and the Nilo alloy codes of samples used to compute the theoretical values for radiation shielding mechanisms.

Table 1. Composition of chemicals and density of Nilo alloy

Fraction of Elements (wt%)	Samples code		
	Nilo alloy 36	**Nilo alloy 42**	**Nilo alloy 48**
	AS1	**AS2**	**AS3**
Ni	38.000	42.000	48.000
Fe	58.900	56.120	49.450
C	0.100	0.050	0.050
Mn	0.600	0.080	0.800
P	0.025	0.025	0.025
S	0.025	0.025	0.025
Si	0.350	0.300	0.300
Cr	0.500	0.250	0.250
Al	-	0.150	0.100
Mo	0.500	-	-
Co	1.000	1.000	1.000
Density (g/cm^3)	8.110	8.110	8.200

Mass attenuation coefficient (MAC), half value layer (HVL), tenth value layer (TVL) and mean free path (MFP)

As shown in Equation (1), the theoretical determination of MAC (cm^2/g) for Nilo alloys samples was calculated using mixing law and assessed using WinXCom at energies range around 1 keV-100 GeV. This software is famous and wildly used, which can be found in many researches (Ravangvong *et al*., 2022c; Sriwongsa *et al*., 2022,):

$$MAC = \sum \mathrm{w_i} (\mu_\mathrm{m})_\mathrm{i} \quad (1)$$

Where w_i and $(\mu_m)_i$ denote fraction by weight and MAC of the i^{th} component elements, respectively.

A thickness of a sample that reduces radiation intensity to 50% and 90% of its initial intensity, respectively, is known as HVL and TVL. These parameters were estimated using the linear attenuation coefficient (μ) equation using in equation (Pires, 2022; Kursun *et al*., 2023; Sreenivas *et al*., 2023; Subedi *et al*., 2023):

$$\mathrm{HVL} = \frac{0.693}{\mu} \quad (2)$$

$$TVL = \frac{\ln 10}{\mu} = \frac{2.302}{\mu} \quad (3)$$

The mean free path (MFP) represents the average particle travel time within the matter prior to collision. It is mostly referred to as relaxation time. Besides, the MFP is inversely proportional to μ value. The formula determining mean free path is according to equation 4 (Ravangvong *et al*., 2023; Lakshminarayana *et al*., 2023):

$$\mathrm{MFP} = \frac{1}{\mu} \quad (4)$$

Buildup factors (BFs)

When assessing shielding, we use a correction term, the buildup factor (B), that accounts for the impact of both secondary photons and scattered radiation inside the irradiated matter. Moreover, the contribution of scattered photons is presented by the buildup factor, which is a unitless multiplicative factor. Hence, this parameter is employed to adjust the response of uncollided photons.

At any given point, the ratio of the total number of photons (primary and secondary) to the photons number that have not collided and are still reaching that same point is known as B. The incident photon energy, target material's thickness, and chemical composition all affect B's value. Additionally, the revised Lambert-Beer law can be expressed as follows:

$$I = BI_0 e^{\mu x} \quad (5)$$

Furthermore, energy absorption buildup factor (EABF) and exposure buildup factor (EBF) are the two types of buildup factors. The first has to do with how energy is deposited or absorbed in the intended material. The second is presented the exposure in air afterward crossing the target matter.

To calculate buildup factors, the following three steps must be followed in order: (1) computing the equivalent atomic number (Z_{eq}); (2) computing the parameters of G-P fitting (appointed by b, c, a, X_k, and d); and (3) computing the buildup factor.

Z_{eq} is a single parameter which explains properties of alloys in terms of equivalent elements and has been computed from ratio of Compton partial mass attenuation coefficient $(\mu_m)_{Compton}$ associate with the total mass attenuation coefficient $(\mu_m)_{Total}$ at same photon energy, using formula:

$$Z_{eq} = \frac{Z_1(\log R_2 - \log R) + Z_2(\log R - \log R_1)}{\log R_2 - \log R_1} \quad (6)$$

where Z_1 and Z_2 are atomic numbers of elements according to ratios R_1 and R_2, respectively. R is the ratio $(\mu_m)_{Compton}/(\mu_m)$Total for alloys at same energy. The parameters of G-P fitting are computed by logarithmic interpolation method for Z_{eq}. The parameters of G-P fitting for elements were taken report by the standard reference database, the American Nuclear Society ANSI/ANS-6.4.3. For alloys was using formula:

$$P = \frac{P_1(\log Z_2 - \log Z_{eq}) + P_2(\log Z_{eq} - \log Z_1)}{\log Z_2 - \log Z_1} \quad (7)$$

where P_1 and P_2 are value of G-P fitting parameters according to atomic numbers of Z_1 and Z_2, respectively at same energy. The parameters of G-P fitting of glasses were used to compute EABF and EBF as determined by:

$$B(E,X) = 1 + \frac{b-1}{K-1}(K^x - 1) \quad \text{for } K \neq 1 \quad (8)$$

$$B(K,X) = 1 + (b-1)x \quad \text{for } K=1 \quad (9)$$

and

$$K(E,x) = cx^a + d\,\frac{\tanh\left(\frac{x}{X_K} - 2\right) - \tanh(-2)}{1 - \tanh(-2)}$$

for $x \leq 40$ mfp (10)

where E and x are incident photon energy and penetration depth in terms of mean free path (mfp), respectively., a, b, c, d, and X_k are G-P fitting parameters. K parameter with deep penetration indicates photon dose multiplication and adjusts in configuration of the spectrum (Ravangvong *et al*., 2022a; Kaur *et al*., 2024; Alda'ajeh *et al*., 2023; Hila *et al*., 2021).

Fast neutron removal cross-section ($\sum_R$)

Neutrons interact with their surroundings through transmission, absorption, and scattering. The possibility of one or more of these processes happening is through the reaction of microscopic cross-section (Lakshminarayana *et al*., 2022, Mhareb *et al*., 2021, Sriwongsa *et al*., 2023).

The fast neutrons (E > 0.1 MeV) $\sum_R$ was estimated using relationship Eq. (6)

$$\sum_R = \sum_i W_i \left(\sum_R / \rho\right)_i \tag{6}$$

Where ρ_{wi} and ρ mean partial density, and total density of the medium, respectively.

Results and Discussion

Mass attenuation coefficient (MAC), half value layer (HVL), tenth value layer (TVL) and mean free path (MFP)

Figure 1 shows the MAC values for Nilo alloy samples as a function of energy. The graph reveals that the MAC values for all samples are large at low energies, then decrease rapidly before gradually increasing as the energy rises. These trends can be explained by the different energy ranges, which are associated with the photoelectric effect (PE), Compton scattering (CS), and pair production (PP) processes. These processes are directly proportional to $E^{-3.5}$, E^{-1}, and log E, respectively (Ravangvong *et al*., 2022b). At low energies, the MAC values exhibit discontinuities due to the K- and L-shell absorption edges of the elements in the alloy samples, which result in the order of MAC values: AS3 < AS2 < AS1 at certain energies. The results indicate that the AS3 alloy sample has the highest MAC value.

The HVL, TVL, and MFP as functions of energy are presented in Figures 2-4. The graphs show that the HVL, TVL, and MFP values for the AS3 alloy are the lowest, which can be attributed to the high nickel content and density of this sample. These results suggest that as nickel content and density increase, the penetrating energy decreases. When comparing the HVL, TVL, and MFP values of the alloy samples (AS1, AS2, and AS3) with hematite serpentine, it was found that all the alloy samples had lower values than hematite serpentine. This indicates that the alloy samples offer better radiation shielding properties than hematite serpentine (Bashter, 1997; Afaneh *et al*., 2022; Acikgoz *et al*., 2023; Al-Hadeethi and Sayyed, 2023; Rouihem *et al*., 2024; Karthika *et al*., 2024).

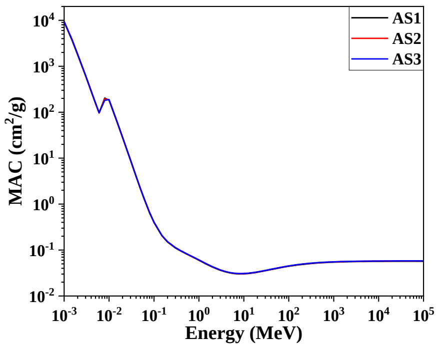

Figure 1. **MAC versus energy for alloy samples**

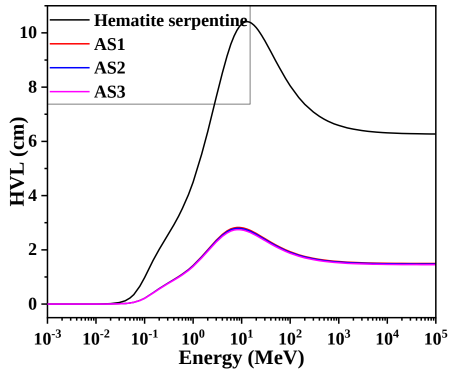

Figure 2. **HVL versus energy for alloy samples**

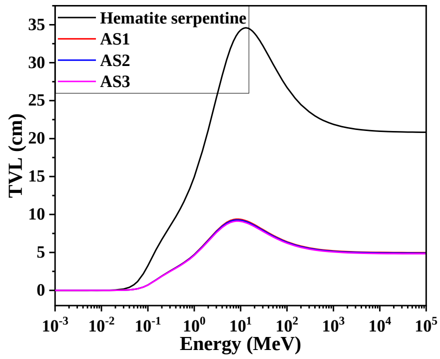

Figure 3. **TVL with energy for alloy samples**

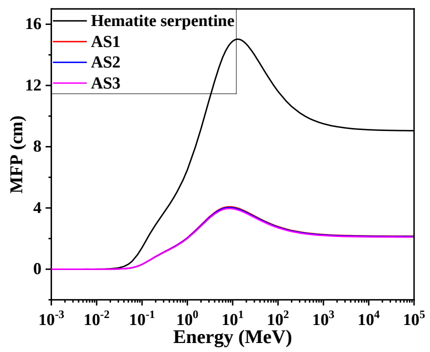

Figure 4. **MFP with energy for alloy samples**

Buildup factors (BFs)

The Z_{eq} quantity is a parameter used to evaluate the BFs (EABF and EBF) values, as shown in Figure 5. The Z_{eq} values are small at low energies (E < 1.00 MeV), increase rapidly in the intermediate energy range, and then decrease at higher energies. These trends correspond to the dominance of the photoelectric effect (PE), Compton scattering (CS), and pair production (PP) processes in the respective energy ranges. The highest Zeq value was observed for the AS3 alloy, which has the highest nickel content and density (Alsaif *et al*., 2021).

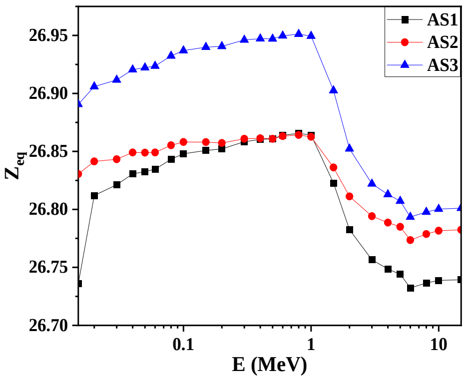

Figure 5. Z_{eq} with energy for alloy samples

EABF and EBF are fundamental values used in planning radiation shielding material properties. These quantities are evaluated based on Z_{eq} and G-P-values, which can be explained in the context of different energy ranges-low, intermediate, and high-where PE, CS, and PP are the dominant processes, respectively. EABF and EBF values for the alloy samples, across energies (0.015-15 MeV) and varying penetration depths (PD), are shown in Figures 6 and 7. It was observed that the EABF and EBF values remain nearly constant at low energies due to the cross-section varying inversely with energy as $E^{-3.5}$. At low energies, the alloy samples absorb the most radiation, resulting in lower EABF and EBF values. At intermediate energies, both values suddenly increase due to photon collisions, reflecting energy loss and prolonged energy collection in the sample. As PD increases, the scattering of photons also increases, leading to a rise in EABF and EBF values, which then decrease at high energies (Alsaif *et al*., 2021; Hila *et al*., 2021; Al-Saeedi *et al*., 2022; Kaur *et al*., 2024).

Figures 8 and 9 illustrate the EABF and EBF values as a function of penetration depth (PD) up to 40 mfp at specific energies of 0.015, 0.15, 1.5, and 15 MeV. It was found that the EABF and EBF values remain nearly constant at 0.015 MeV, then increase with increasing PD at energies of 0.15-15 MeV. This behavior is attributed to the dominant interaction processes at each energy, as mentioned earlier (Sayyed *et al*., 2018; Alsaif *et al*., 2021; Alsaif *et al*., 2023).

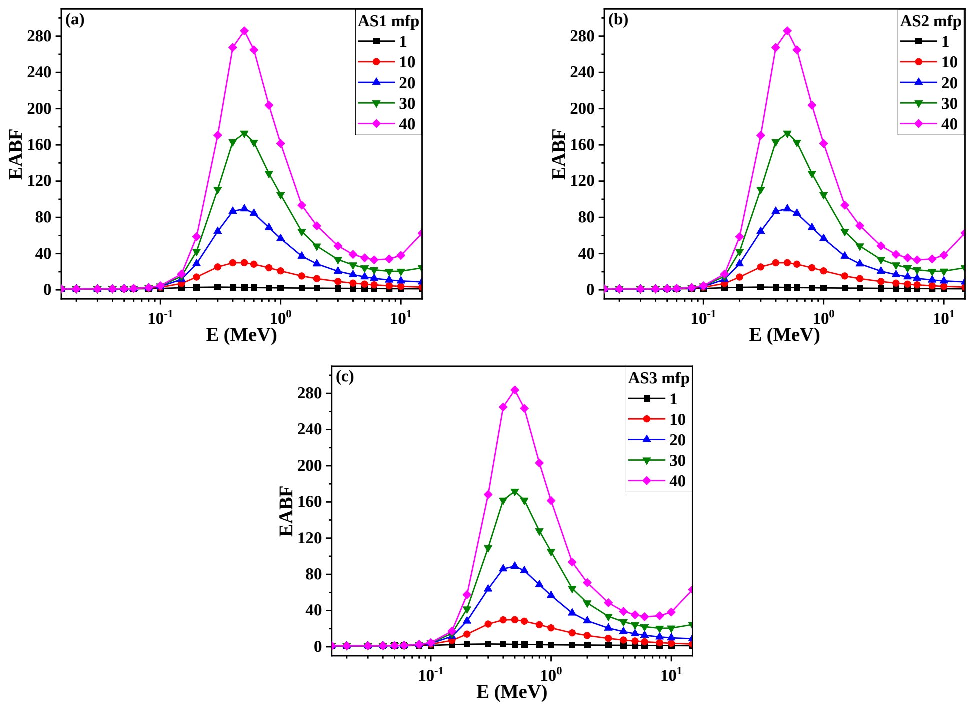

Figure 6. (a-c) EABF with energies ranging from 0.015-15 MeV until 40 mfp for alloy samples

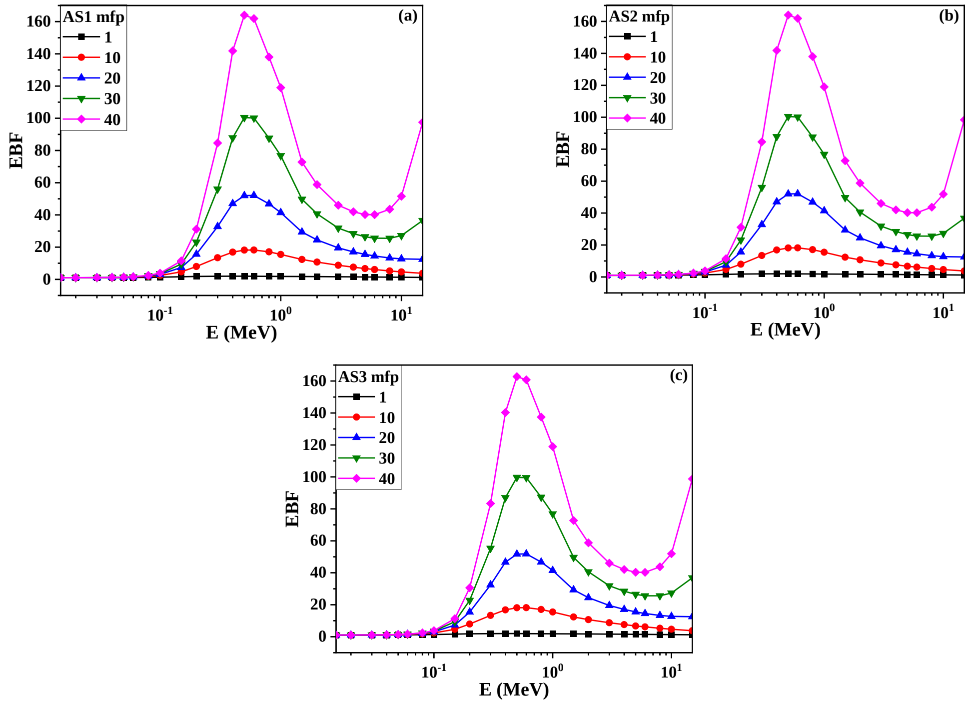

Figure 7. (a-c) EBF VS energies ranging 0.015-15 MeV until 40 mfp for alloy samples

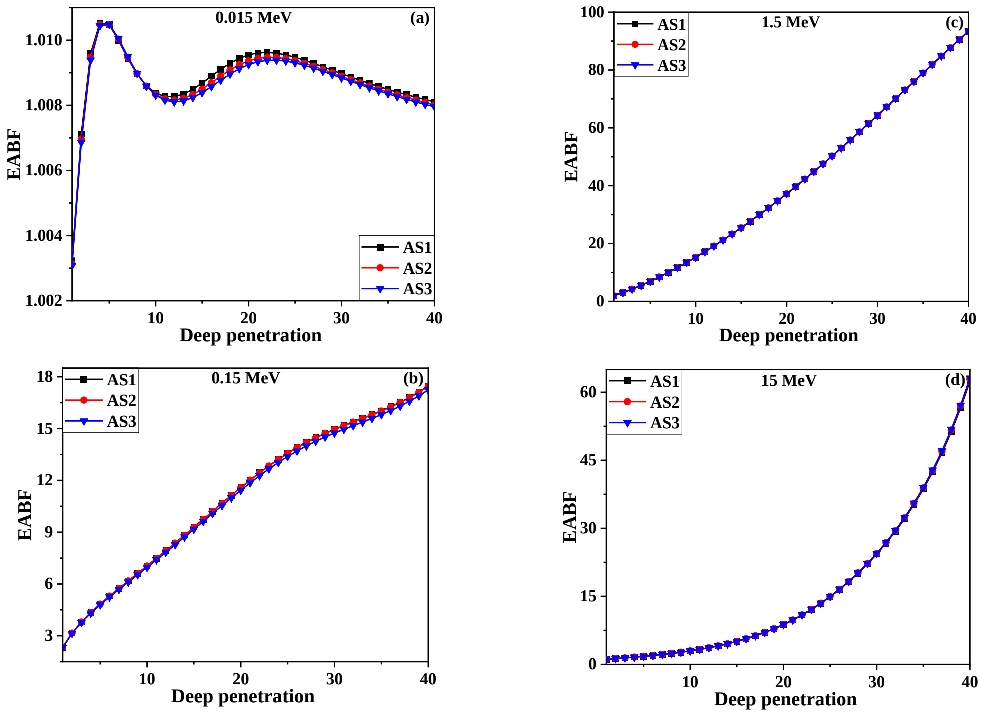

Figure 8. (a-d) EABF for alloy samples until 40 mfp at specific energies

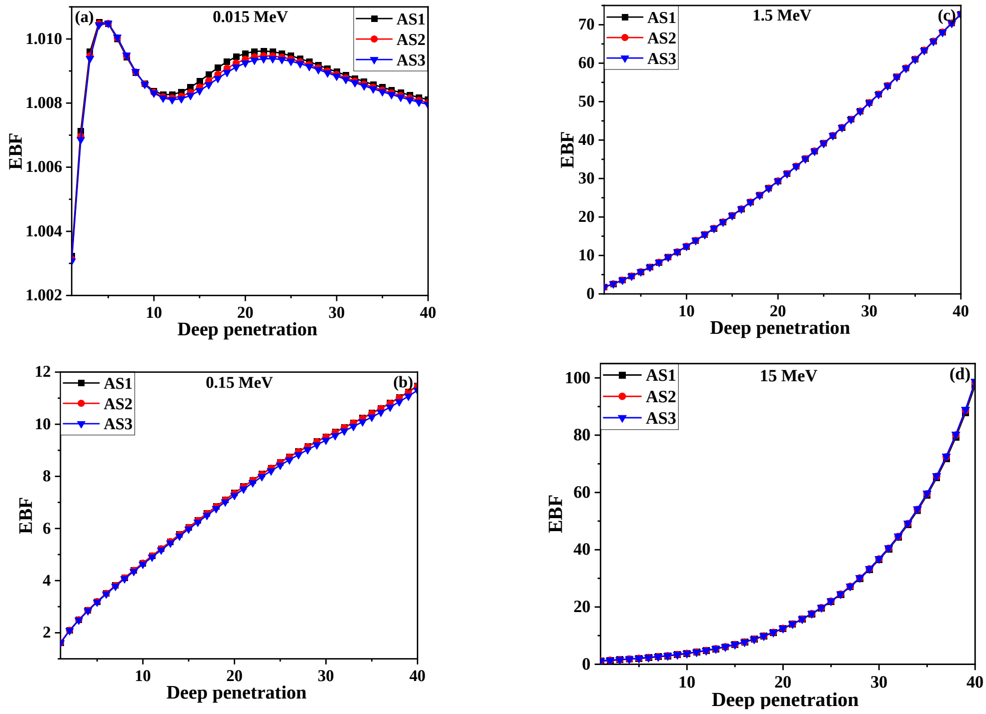

Figure 9. (a-d) EBF for alloy samples until 40 mfp at specific energies

Fast neutron removal cross-section; Σ_R

The fast neutron shielding capability of an alloy refers to the probability that a fast neutron undergoes a first collision, effectively removing it from the group of penetrating, uncollided neutrons. This property is essential for measuring the neutron-absorbing capacity of any material and is represented by the removal cross-section (Σ_R), as shown in Figure 10. It was found that the AS3 alloy sample had the highest Σ_R value, which can be attributed to its higher density. This indicates that the AS3 alloy is particularly effective at shielding fast neutrons (Sayyed *et al*., 2020; Effendy *et al*., 2021).

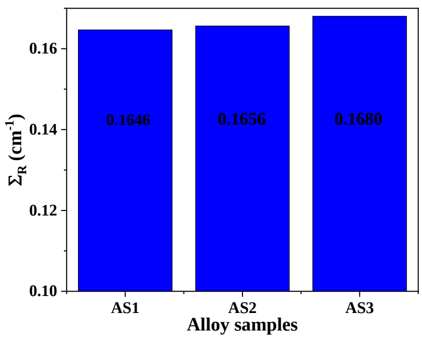

Figure 10. The fast neutron removal cross-section for Nilo alloys

Conclusions

This work explained the radiation and fast neutron shielding properties of Nilo alloys with compositions 36, 42, and 48. The radiation shielding properties included the mass attenuation coefficient (MAC), half value layer (HVL), tenth value layer (TVL), mean free path (MFP), and buildup factors (BFs), while the fast neutron shielding property is described by the fast neutron removal cross-section. The results for radiation shielding properties across the energy range from 1 keV to 105 MeV show that the AS3 alloy sample had the highest MAC value, while its HVL, TVL, and MFP values were the lowest. Additionally, when comparing HVL, TVL, and MFP values between the alloy samples and hematite serpentine, the alloy samples exhibited lower values than hematite serpentine due to they had higher than density. For the BFs in the energy range of 0.015-15 MeV, the AS3 alloy showed the highest BFs values. Furthermore, the fast neutron shielding properties of the AS3 alloy were also the best, as it had the highest fast neutron removal cross-section. These results suggest that the AS3 alloy is highly effective for both radiation and fast neutron shielding, making it a promising candidate for developing Pb-free materials.

Acknowledgment

This research was accomplished due to the cooperation of Nakhon Pathom Rajabhat University, Silpakorn University and Phetchaburi Rajabhat University.

References

Acikgoz, A., Aladailah, M.W., Tashlykov, O.L., Demircan, G., Kamislioglu, M., Yasar, M.M., Hozdogan, H., and Yorulmaz, N. (2023). Influence of Nd_2O_3 on radiation shielding and elastic properties of TeO_2-MgO-Na_2O glasses: A simulation study by PHITS and MCNP. Pramana, 97(167):1-13. https://doi.org/10.1007/s12043-023-02629-7

Afaneh, F., Khattari, Z.Y., and Al-Buriahi, M.S. (2022). Monte Carlo simulations and phy-X/PSD study of radiation shielding and elastic effects of molybdenum and tungsten in phosphate glasses. Journal of Materials Research and Technology, 19:3788-3802. https://doi.org/10.1016/j.jmrt.2022.06.125

Alda'ajeh, M.M., Sharaf, J.M., Saleh, H.H., and Hamideen, M.S. (2023). Determination of buildup factors for some human tissues using both MCNP5 and Phy-X / PSD. Nuclear Engineering and Technology, 55(12):4426-4430. https://doi.org/10.1016/j.net.2023.08.025

Aldawood, S., Asemi, N.N., Kassim, H., Aziz, A.A., Saeed, W.S., and Al-Odayni, A.B. (2024). Gamma radiation shielding by titanium alloy reinforced by polymeric composite materials. Journal of Radiation Research and Applied Sciences, 17(1):100793. https://doi.org/10.1016/j.jrras.2023.100793

Al-Hadeethi, Y., and Sayyed, M.I. (2023). Correlation between the concentration of TeO_2 and the radiation shielding properties in the TeO_2-MoO_3-V_2O_5 glass system. Nuclear Engineering and Technology, 55(4):1218-1224. https://doi.org/10.1016/j.net.2022.12.014

Al-Saeedi, F.H.F., Sayyed, M.I., Kapustin, F.L., Al-Ghamdi, H., Kolobkova, E.V., Tashlykov, O.L., Almuqrin, A.H., and Mahmoud, K.A. (2022). A novel barium oxide-based Iraqi sand glass to attenuate the low gamma-ray energies: Fabrication, mechanical, and radiation protection capacity evaluation. Nuclear Engineering and Technology, 54(8):3051-3058. https://doi.org/10.1016/j.net.2022.03.016

Alsaif, N.A.M., Elmahroug, Y., Alotaibi, B.M., Alyousef, H.A., Rekik, N., Hussein, W.M.A., Chand, R., and Farooq, U. (2021). Calculating photon buildup factors in determining the γ-ray shielding effectiveness of some materials susceptible to be used for the conception of neutrons and γ-ray shielding. Journal of Materials Research and Technology, 11:769-784. https://doi.org/10.1016/j.jmrt.2021.01.052

Alsaif, N.M.A., Khattari, Z.Y., Zakaly, H.M.H., Rammah, Y.S., Ene, A., and Al-Buriahi, M.S. (2023). Mechanical-elastic properties and radiation attenuation efficiency of TeO_2/WO_3/K_2O composite glass systems for nuclear and medical applications. Heliyon, 9(8):e18912. https://doi.org/10.1016/j.heliyon.2023.e18912

Aygün, B. (2021). Neutron and gamma radiation shielding Ni-based new type super alloys development and production by Monte Carlo Simulation technique. Radiation Physics and Chemistry, 188:109630. https://doi.org/10.1016/j.radphyschem.2021.109630

Bashter, I.I. (1997). Calculation of radiation attenuation coefficients for shielding concretes. Annals of Nuclear Energy, 24(17):1389-1401. https://doi.org/10.1016/S0306-4549(97)00003-0

Cheng, B., Huang, X., Zhang, M., Mao, C., Wu, D., Zhou, D., Ma, G., Tang, K., and Luo, B. (2024). Microstructure and properties of laser welding Ni-based alloy/austenitic stainless steel with filler wire for nuclear reactor pump can end sealing. Journal of Materials Research and Technology, 30:1929-1938. https://doi.org/10.1016/j.jmrt.2024.03.239

Effendy, N., Zaid, M.H.M., Sidek, H.A.A., Matori, K.A., Mahmoud, K.A., and Sayyed, M.I. (2021). Influence of ZnO to the physical, elastic, and gamma radiation shielding properties of the tellurite glass system using MCNP-5 simulation code. Radiation Physics and Chemistry, 188:109665. https://doi.org/10.1016/j.radphyschem.2021.109665

Ekinci, N., El-Agawany, F.I., Mahmoud, K.A., Karabulut, A., Aygün, B., Yousef, E., and Rammah, Y.S. (2021). Synthesis, physical properties, and gamma-ray shielding capacity of different Ni-based super alloys. Radiation Physics and Chemistry, 186:109483. https://doi.org/10.1016/j.radphyschem.2021.109483

Fernandes, M.T., Silva, L.M., Mendes, P.S.N., Queiroz, A.V., Castro, J.A., and Santos, C. (2021). A degradation kinetics model of Mg-Zn-Mn-Ca alloys in Kokubo solution. Journal of Materials Research and Technology, 11:887-895. https://doi.org/10.1016/j.jmrt.2021.01.063

Hila, F.C., Hila, A.M.V.J., Sayyed, M.I., Astronomo, A.A., Dicen, G.P., Jecong, J.F.M., Guillermo, N.R.D., and Amorsolo Jr, A.V. (2021). Evaluation of photon radiation attenuation and buildup factors for energy absorption and exposure in some soils using EPICS2017 library. Nuclear Engineering and Technology, 53(11):3808-3815. https://doi.org/10.1016/j.net.2021.05.030

Huang, Y.J., Zhang, F.L., Pan, X.Y., Gao, P., Zheng, C.J., Zhou, Y.M., and Li, H.B. (2024). Fabrication and evaluation of high-entropy alloy reinforced Fe bond diamond tool. Journal of Materials Processing Technology, 328:118419. https://doi.org/10.1016/j.jmatprotec.2024.118419

Karthika, S., Sundari, S.S., Marimuthu, K., and Meena, P. (2024). Enhancement of electrical and radiation shielding properties of vanadium-doped lithium telluro-borate (LTB) glasses. Chemistry Physics Impact, 8:100430. https://doi.org/10.1016/j.chphi.2023.100430

Kaur, K., Karol, V., Kumar, P., Kaur, G., Sharma, P., Saroa, A., and Singh, A. (2024). Energy build-up factors estimation for $BaZr_{0.10}Ti_{0.90}O_3$, $Ba_{0.90}La_{0.10}TiO_3$, and $Ba_{0.90}La_{0.10}Zr_{0.10}Ti_{0.90}O_3$ ceramics in shielding applications. Nuclear Engineering and Technology, 56(5):1822-1829. https://doi.org/10.1016/j.net.2023.12.039

Khakwani, S. (2024). Magnetic characterization of HPT-deformed Fe-Si soft magnetic alloys before and after heat treatment and internal stress calculations. Physica B: Condensed Matter, 685:416017. https://doi.org/10.1016/j.physb.2024.416017

Kursun, C., Gao, M., Guclu, S., Gaylan, Y., Parrey, K.A., and Yalcin, A.O. (2023). Measurement on the neutron and gamma radiation shielding performance of boron-doped titanium alloy Ti50Cu30Zr15B5 via arc melting technique. Heliyon, 9(11):e21696. https://doi.org/10.1016/j.heliyon.2023.e21696

Lakshminarayana, G., Dong, M.G., Al-Buriahi, M.S., Rekik, N., Lee, D.E., Yoon, J., and Park, T. (2023). Physical, structural, thermal, and mechanical features combined with neutron and gamma radiation attenuation qualities of Sm_2O_3 doped transparent borate-rich glasses. Journal of Materials Research and Technology, 22:1268-1296. https://doi.org/10.1016/j.jmrt.2022.11.177

Lakshminarayana, G., Tekin, H.O., Dong, M.G., Al-Buriahi, M.S., Lee, D.E., Yoon, J., and Park, T. (2022). Comparative assessment of fast and thermal neutrons and gamma radiation protection qualities combined with mechanical factors of different borate-based glass systems. Results in Physics, 37:105527. https://doi.org/10.1016/j.rinp.2022.105527

Liu, P., Huang, Q., Shan, Q., Jiao, Z., Wang, Q., Ma, Y., Zhou, R., Baker, I., and Wu, H. (2024a). Achieving exceptional work-hardening capability of additively-manufactured multiphase Fe-Mn alloys via multiple deformation mechanisms. International Journal of Plasticity, 173:103871.

Liu, S., Wang, R., Wang, L., Ge, F., Gao, M., Si, Y., and Li, B. (2024b). Corrosion behavior of iron-based and Ni-based alloys melted in NaCl-$MgCl_2$-KCl mixed molten salt under vacuum atmosphere. Journal of Materials Research and Technology, 28:1915-1923. https://doi.org/10.1016/j.jmrt.2023.12.121

Mhareb, M.H.A., Alajerami, Y.S.M., Dwaikat, N., Al-Buriahi, M.S., Alqahtani, M., Alshahri, F., Saleh, N., Alonizan, N., Saleh, M.A., and Sayyed, M.I. (2021). Investigation of photon, neutron, and proton shielding features of H_3BO_3-ZnO-Na_2O-BaO glass system. Nuclear Engineering and Technology, 53(3):949-959. https://doi.org/10.1016/j.net.2020.07.035

Padhy, S.P., Chaudhary, V., Lim, Y.F., Zhu, R., Thway, M., Hippalgaonkar, K., and Ramanujan, R.V. (2024). Experimentally validated inverse design of multi-property Fe-Co-Ni alloys. iScience, 27(5):109723. https://doi.org/10.1016/j.isci.2024.109723

Pan, J., Wang, C., Wang, Z., Zhang, C., Fang, L., Li, J., Mei, Q., Gao, J., Wang, M., Li, H., Wu, Z., and Xiao, X. (2024). Microstructure characteristics and properties of a novel Ni-based alloy for thermal neutron and gamma ray co-shielding. Materials Characterization, 210:113840. https://doi.org/10.1016/j.matchar.2024.113840

Pires, L.F. (2022). Radiation shielding properties of weathered soils: Influence of the chemical composition and granulometric fractions. Nuclear Engineering and Technology, 54(9):3470-3477. https://doi.org/10.1016/j.net.2022.04.002

Ravangvong, S., Glumglomchit, P., Zuprakhon, S., Thinkoksoong, T., Jitrawang, P., Sriwongsa, K., Khobkham, C., and Kaewkhao, J. (2023). The properties of Bi_2O_3 additive on radiation shielding and elastic moduli properties of TeO_2-P_2O_5 based glass system. Integration Ferroelectrics, 238(1):280-295. https://doi.org/10.1080/10584587.2023.2234576

Ravangvong, S., Nisspa, W., Glumglomchit, P., Amornsophon, P., Kanuenghet, R., Pakdeepensuk, P., Sriwongsa, K., Khobkham, C., and Kaewkhao, J. (2022a). Effects of WO_3 on radiation shielding properties of WO_3-TeO_2 binary tellurite glass system. Integration Ferroelectrics, 222(1):125-135. https://doi.org/10.1080/10584587.2021.1961522

Ravangvong, S., Sriwongsa, K., Glumglomchit, P., Phamornsut, K., Yampichai, N., Tantiwatcharakultorn, A., Sangngoen, S., and Kaewkhao, J. (2022b). Behaviors of TeO_2-B_2O_3-WO_3 glass system for ionizing radiation shielding performance: Photon, protons and alpha particles. Materials Today: Proceedings, 65(Part 4):2269-2276. https://doi.org/10.1016/j.matpr.2022.04.005

Ravangvong, S., Sriwongsa, K., Glumglomchit, P., Suksee, N., Kaewket, P., Katekeaw, W., Nisspa, W., and Kaewkhao, J. (2022c). The impact on addition of WO_3 for radiation shielding properties of TeO_2-BaO glass system. Integration Ferroelectrics, 224(1):134-144. https://doi.org/10.1080/10584587.2022.2035603

Rouihem, F., Albarqi, M.M., Alsulami, R.A., and Hosni, F. (2024). Lead-free gamma-ray shielding: Comparative analysis of elastomeric and fluoro-rubber materials using FLUKA and EGSnrc simulations. Journal of Radiation Research and Applied Sciences, 17(1):100834. https://doi.org/10.1016/j.jrras.2024.100834

Saleh, A., Mansour, F.E., and Abdelhakim, N.A. (2024). An appropriate balance of mechanical and ionized radiation shielding performance across some tin binary alloys: A comparative investigation. Radiation Physics and Chemistry, 221:111726. https://doi.org/10.1016/j.radphyschem.2024.111726

Saleh, A., Shalaby, R.M., and Abdelhakim, N.A. (2022). Comprehensive study on structure, mechanical and nuclear shielding properties of lead free Sn-Zn-Bi alloys as a powerful radiation and neutron shielding material. Radiation Physics and Chemistry, 195:110065. https://doi.org/10.1016/j.radphyschem.2022.110065

Sayyed, M.I., AlZaatreh, M.Y., Matori, K.A., Sidek, H.A.A., and Zaid, M.H.M. (2018). Comprehensive study on estimation of gamma-ray exposure buildup factors for smart polymers as a potent application in nuclear industries. Results in Physics, 9:585-592. https://doi.org/10.1016/j.rinp.2018.01.057

Sayyed, M.I., Kumar, A., Tekin, H.O., Kaur, R., Singh, M., Agar, O., and Khandaker, M.U. (2020). Evaluation of gamma-ray and neutron shielding features of heavy metals doped Bi_2O_3-BaO-Na_2O-MgO-B_2O_3 glass systems. Progress in Nuclear Energy, 118:103118. https://doi.org/10.1016/j.pnucene.2019.103118

Sreenivas, B., Ahmmad, S.K., Rammah, Y.S., and Bindu, P.H. (2023). Radiation shielding capacity and machine learning density prediction of boro-bismuth cadmium zinc glasses. Open Ceramics, 16:100493. https://doi.org/10.1016/j.oceram.2023.100493

Sriwongsa, K., Sawatchai, S., Neawhengtham, S., Anuntabundit, N., Daocharern, P., Glumglomchit, P., Wisitrungsee, K., Ravangvong, S., Chaiphaksa, W., and Kaewkhao, J. (2023). The investigation optical, X/γ-rays and neutrons shielding properties of BaO based on steel slag glass system. Integration Ferroelectrics, 238(1):246-261. https://doi.org/10.1080/10584587.2023.2234573

Sriwongsa, K., Sirimongkolchaikul, J., Sukrasorn, C., Bussaparoek, T., Kanunghet, S., Phansuea, T., Glumglomchit, P., Limkitjaroenporn, P., and Kaewkhao, J. (2022). Radiation and fast neutron shielding properties of nickel-based superalloys: Inconel 600, 718, and 725 superalloys. Integration Ferroelectrics, 224(1):120-133. https://doi.org/10.1080/10584587.2022.2035602

Subedi, B., Paudel, J., and Lamichhane, T.R. (2023). Gamma-ray, fast neutron and ion shielding characteristics of low-density and high-entropy Mg-Al-Ti-V-Cr-Fe-Zr-Nb alloy systems using Phy-X/PSD and SRIM programs. Heliyon, 9(7):e17725. https://doi.org/10.1016/j.heliyon.2023.e17725

Wu, J., Hu, J., Deng, Z., Feng, Y., Zhao, X., Fan, H., Wang, Z., Zhang, W., and Wang, K. (2023). Ga-In-Sn-Bi alloys for radiation shielding application: Investigation of the structures, morphologies, and X-ray attenuation performances. Journal of Alloys and Compounds, 969:172294. https://doi.org/10.1016/j.jallcom.2023.172294

Xu, K., Jiang, H., Yan, J.B., Zhang, P., Liu, P., Cao, G.H., and Yuan, Y. (2023). Tensile properties and deformation mechanisms of a solution treated Ni-Fe-based alloy at high temperatures. Materials Science and Engineering, 881:145418. https://doi.org/10.1016/j.msea.2023.145418

Yaykaşlı, H., Eskalen, H., Kavun, Y., Göğebakan, M., Kaya, A.H., and Yorulmaz, N. (2023). CoCrFeNiSi high entropy alloy: Synthesis, structural and radiation shielding properties. Progress in Nuclear Energy, 165:104930. https://doi.org/10.1016/j.pnucene.2023.104930